Int. J. Multiphase Flow Vol. 11, No. 3, pp. 317–345, 1985
Printed in the U.S.A.

0801–9322/85 $3.00 + .00

VOID FRACTION, BUBBLE VELOCITY AND BUBBLE SIZE IN TWO-PHASE FLOW

R. VAN DER WELLE†
Laboratory for Thermal Power Engineering, Delft University of Technology, Delft, The Netherlands

(*Received* 15 *August* 1983; *in revised form* 15 *August* 1984)

Abstract—Experiments were performed in atmospheric vertical air–water flows, for void fractions between 0.25 and 0.75 (cross-sectional averages) and superficial liquid velocities of 1.3, 1.7 and 2.1 m/s. Local values of void fraction and bubble velocity as well as the bubble diameter were measured by means of a resistivity probe technique. Reliable values were obtained for the local void fraction over the entire range $0 \leq \alpha \leq 1$. The void fraction profiles appeared to have a local maximum at the pipe center, local maxima close to the wall were obviously absent. The resistivity probes are shown to measure the velocity of the interface between the conducting and nonconducting phases, which equals the gas velocity only for low void fractions. The measured data for void fraction and bubble velocity were correlated by means of power law distribution functions, with exponents given by a function of the cross-sectionally averaged void fraction. The Sauter mean diameters for the bubble size spectra found, agree reasonably well with diameters predicted by a theoretical model based on the energy dissipation in the flow.

1. INTRODUCTION

Various measuring methods were considered at the outset, taking account of related experience in the author's laboratory and of the relevant literature, such as the review on two-phase flow measuring techniques given by Jones & Delhaye (1976). One of the requirements for a suitable measuring method would be the absence of obstructions in the flow channel. Two methods meet this requirement, viz. the γ-ray attenuation technique and laser-Doppler anemometry. However, the former yields only a chord-averaged value of the void fraction, while the latter is so far only applicable in cases where the discrete phase is sufficiently dilute, i.e. for low void fractions. In view of the intention to measure local variables in flows with void fractions possibly ranging from zero to unity it was inevitable to use a probe technique. An evaluation of potential probe techniques resulted in the selection of the electrical resistivity probe because of the relatively simple equipment and the positive results for conducting liquids reported in the literature.

The first references found on the use of the resistivity probe technique were Neal (1963), for measurements in mercury–nitrogen flow, and Nassos (1963), for air–water mixtures. Since that time a number of investigators have reported on the use of such probes for the measurement of local properties in gas–liquid flows. Some measurements were limited to void fractions, see, e.g. Malnes (1966), and Zwahr (1976); others, like Neal & Bankoff (1963), Herringe & Davis (1974, 1976), Serizawa *et al.* (1975) and Thang & Davis (1979), have used two probes in series, combined with a correlation technique, to measure bubble sizes and bubble velocities. In the present investigation the technique was employed to determine void fraction, bubble velocity and bubble size.

In addition, chord-average void fractions were determined by the γ-ray technique, while temperatures and pressures were measured using conventional equipment.

2. RESISTIVITY PROBE MEASURING TECHNIQUES

2.1. *Measuring principle*

The principle of two-phase flow measurements by resistivity probe is based upon the difference in conductivity between the gaseous and liquid phases. In an air–water flow the air

†Present address: Netherlands Organization for Applied Scientific Research—TNO, P.O. Box 342 7300 AH, Apeldoorn, The Netherlands.

can be considered as electrically insulating, whereas demineralized water has a conductivity of about 10 μS/m. When the sensor is in contact with the continuous liquid the circuit is closed, whereas a bubble will break the circuit. Thus the probe behaves in principle like a switch, yielding a two-state signal. Such a signal shows a nearly immediate response to water contact with the probe, but a delayed response to bubble contact, due to the required dewetting time of the probe tip. Minimization of this delay, i.e. approximation of a square wave shape, is desirable for further processing, and may be obtained by proper design of the probe tip. However, to obtain a true square wave electronic signal processing is also required.

The following three variables can be measured:

—the void fraction α, by determination of the presence of the gas phase
—the bubble size distribution, by classification of the square wave lengths
—the velocity of the bubbles, from the delay time of the bubbles between two probes.

The large amount of data to be processed combined with the desirability of local processing resulted in the decision to use a dedicated microprocessor. This microcomputer system and the software used have been described in detail by Korving (1979).

2.2. *Probe design*

The design proposed by Zwahr (1976) and shown in figure 1 was used to obtain rapid dewetting of the probe tip. It consists of a platinum wire of about 30 μm diameter, insulated by glass except at the front end. The tip of the probe has to be sharp in order to achieve immediate piercing with little deformation of the bubble at the moment of contact. As the contact area consists only of the cross section of the wire, rapid dewetting occurs as the bubble is touched.

Two separate sensor tips are used for determination of bubble velocities. As shown in figure 1, the two sensors have a common stainless steel sheath to maintain a well defined sensor distance and for easy handling.

Preliminary experiments indicated that the distance between the two probe tips should be less than 20 mm to avoid the loss of correlation between the signals due to turbulence. Nor should the distance be too small, as in that case determination of the time delay becomes inaccurate. The most suitable distance between the tips was found to be about 10 mm.

2.3. *Signal conditioning and processing*

Two consecutive steps should be distinguished, viz. signal conditioning by conversion of the analog signal to a square wave form, and signal processing by sampling of this converted signal.

In the first step all the information contained in the original signal must be converted into information suitable for subsequent handling by a digital microprocessor. In the course of the experiments it was found necessary to apply several improvements to this step in order to achieve the desired reliability and accuracy of the results. At first, use was made of a single

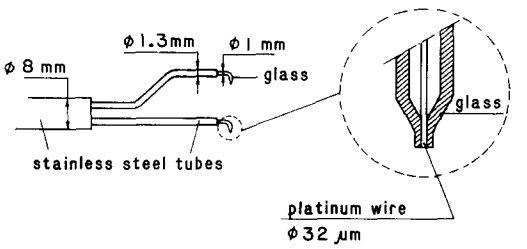

Figure 1. Probe geometry.

trigger level, i.e. an electronic switch was triggered if the voltage reached a value above a preset level. This approach has the inherent disadvantage that signals which do not reach the trigger voltage go undetected. Hence the level must be set as close to the signal voltage as possible, in order to minimize the influence of the dewetting time and to take account of small bubbles. However, the trigger level is now at the wrong side when high void fractions are measured. The problem is further enhanced in practice by shifts in the level of the signal voltage due to fouling of the probe tips and variations in the conductivity of the water.

These disadvantages are avoided by first sampling the signal by an analog-digital converter and then comparing the samples with two self-adjusting trigger levels. The implementation of this approach is illustrated in the block diagram and condition table of figure 2. There are four registers, which contain the samples n, n-1 and a current minimum

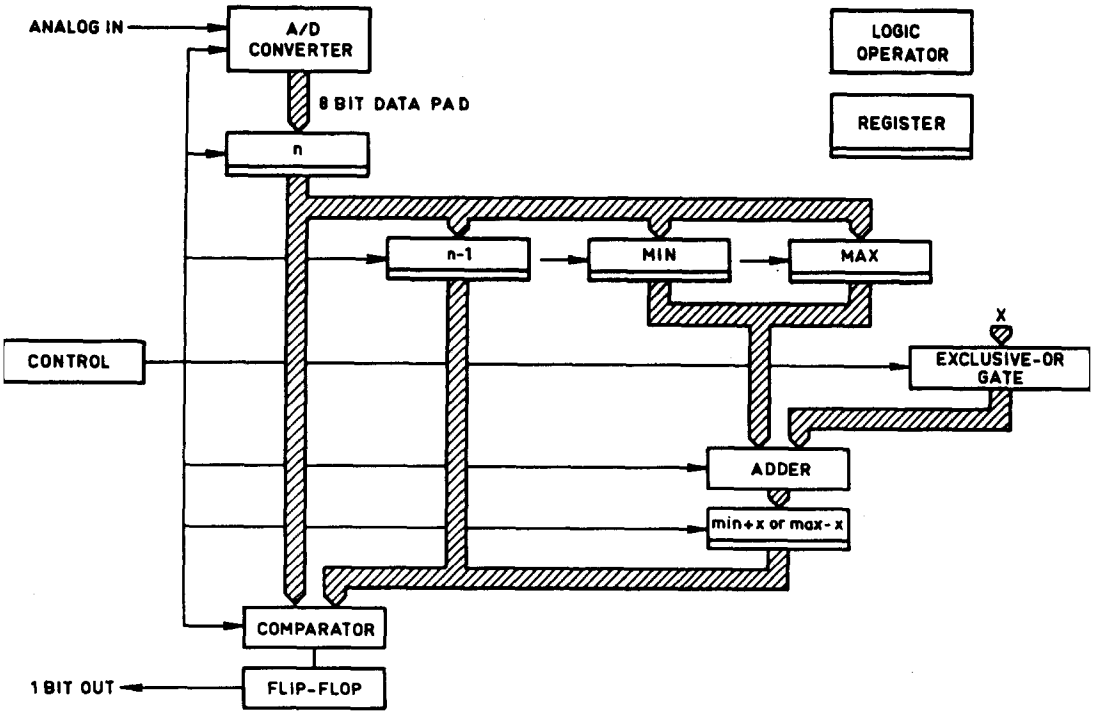

condition	minimum	maximum	output
n > n - 1	q	n	q
n = n - 1	q	q	q
n < n - 1	n	q	q
n > min + x	n	n	1 ↑
n < max - x	n	n	0 ↓

q = no change

Figure 2. Block scheme and condition table of A/D signal conversion.

and maximum value. Sample n is compared with sample n-1 as well as with the minimum and maximum values (cf. the condition table). If either of these values is exceeded one or both limits are adjusted according to the last measured value n, and/or a set or reset of the flip–flop at the output occurs, resulting in the desired square wave signal. Spurious triggering due to noise is avoided by setting an adjustable margin of x bits with respect to both limits. To match the high conversion speed of the A/D converter (sample frequency of 250 kHz), the subsequent arithmetic operations are carried out by TTL hardware, driven by the clock of the A/D converter. All operations can be executed within the conversion time of the A/D converter, permitting simultaneous processing. A more detailed description of the conditioning operation is given by Korving (1980).

Subsequent digital processing of the resulting square wave signal consists of *sampling* the square wave form at a frequency adjustable between 1 and 16 kHz. The maximum value of this frequency is more or less prescribed by the hard- and software capabilities of the processing equipment. The sampling results in a number of zero's and one's representing the square wave in digital form.

2.4. *Applications*

2.4.1. *Void fraction.* The local void fraction, which is measured by the lower of the two sensor tips, is defined as a time average of the concentration c by

$$\alpha = \lim_{T\to\infty} \frac{1}{T} \int_0^T c(x, t)\, \mathrm{d}t \qquad [1]$$

in which c as a function of place x and time t equals one if the phase at the probe tip is gas and zero if the tip is in the liquid phase. As the signal is given in discrete digital form, [1] can be written as

$$\alpha = \frac{1}{N} \sum_{i=1}^{N} a(i) \qquad [2]$$

in which N is the total number of samples and $a(i)$ the number of samples indicating the presence of gas at the probe tip, with both N and $a(i)$ referring to the sampling time T.

2.4.2. *Bubble velocity.* The bubble velocity is determined from the signals of two probes placed in series (cf. figure 3). A bubble which contacts the first probe will in general subsequently make contact with the second probe: the time delay between these two contact signals is a measure for the velocity of the bubble. It is of course possible that a bubble is only pierced by one of the probes, this error source should not cause any problems provided this stochastic process is observed over an adequate length of time. A correlation technique will be required to determine the most probable time delay between the two stochastic signals. The cross-correlation function of the two probe signals a and b is defined by

$$F_{ab}(x, \tau) = \lim_{T\to\infty} \frac{1}{T} \int_0^T a(x, t)\, b(x + d, t + \tau)\, \mathrm{d}t, \qquad [3]$$

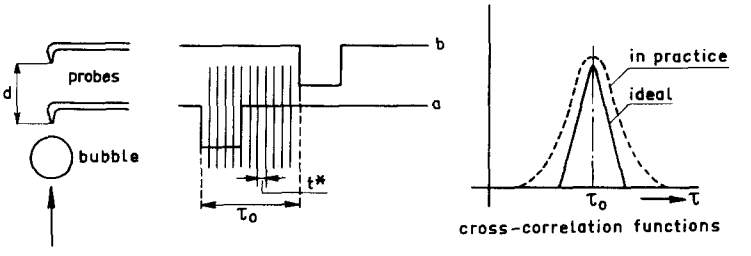

Figure 3. Measurement of bubble velocity.

where d is the distance between the probes and τ is the time delay. The maximum of the correlation function yields the most probable time delay τ_0, from which the bubble velocity is determined as

$$u_G = d/\tau_0. \qquad [4]$$

In the case of binary signals, i.e. when the signals have a resolution of one bit, the correlation function is changed into a polarity correlation function, defined by [cf. e.g. Veltman *et al.* (1961)]

$$R_{ab}(x, \tau) = \lim_{T\to\infty} \int_0^T \operatorname{sgn} a(x, t) \operatorname{sgn} b(x + d, t + \tau)\, \mathrm{d}t, \qquad [5]$$

where the signum function is defined as sgn $y = 1$ if $y \geq 0$ and sgn $y = -1$ if $y < 0$. For a sampled signal between 0 and 1 the signum function is changed into the exclusive-or function $\oplus$ and [5] is written as

$$R_{ab}(x, j) = \sum_{i=1}^{N} a(x, i) \oplus b(x + d, i + j) \qquad [6]$$

and $j = 1\ (1)\ M$,
where N = number of samples, M = number of shifts, and $\oplus$ is defined by

a	b	a $\oplus$ b
0	0	1
0	1	0
1	0	0
1	1	1

Preliminary experiments have shown that for the range of velocities and bubble sizes of interest a good correlation is obtained for $N = 1000$ and $M = 50$.

Figure 4 shows an example of a polarity correlation for two identical signals a and b, sampled with a sampling period t^* indicated in figure 3. These signals are shifted relative to each other and the exclusive-or operation is applied, yielding the expected triangular shaped cross-correlation function. In case of nonidentical signals, i.e. when the width of the blocks differs, the top of the correlation function is broadened (cf. Serizawa *et al.* 1975), which may generate difficulties in determining τ_0. In practice, however, the correlation functions show a single maximum, the place of which is given by the number j. It can be shown (Van der Welle 1983) that the error in j is inversely proportional to the number of samples within the time delay τ_0; i.a.v. if the sampling frequency is sufficiently large, the error in the measured velocity can be kept sufficiently low.

2.4.3. *Bubble diameter.* The chord length l of a bubble follows from the block length of the square wave signal, i.e. from the number of continuous zero samples n, and from the bubble velocity u_G, obtained from [4]:

$$l = \frac{n\, u_G}{f}, \qquad [7]$$

where f is the sampling frequency.

Bubble size data are usually presented in graphical form by means of a distribution function, from which a mean diameter of some sort and a measure of the dispersion of the spectrum can then be derived. The simplest distribution function is a histogram or

a	b	a ⊕ b
0	0	1
0	0	1
0	0	1
1	0	0
1	0	0
1	0	0
0	1	0
0	1	0
0	1	0
j=1		R=3

a	b	a ⊕ b
0	0	1
0	0	1
0	0	1
1	0	0
1	0	0
1	1	1
0	1	0
0	1	0
0	0	1
j=2		R=5

a	b	a ⊕ b
0	0	1
0	0	1
0	0	1
1	0	0
1	1	1
1	1	1
0	1	0
0	0	1
0	0	1
j=3		R=7

a	b	a ⊕ b
0	0	1
0	0	1
0	0	1
1	1	1
1	1	1
1	1	1
0	0	1
0	0	1
0	0	1
j=4		R=9

a	b	a ⊕ b
0	0	1
0	0	1
0	1	0
1	1	1
1	1	1
1	0	0
0	0	1
0	0	1
0	0	1
j=5		R=7

a	b	a ⊕ b
0	0	1
0	1	0
0	1	0
1	1	1
1	0	0
1	0	0
0	0	1
0	0	1
0	0	1
j=6		R=5

a	b	a ⊕ b
0	1	0
0	1	0
0	1	0
1	0	0
1	0	0
1	0	0
0	0	1
0	0	1
0	0	1
j=7		R=3

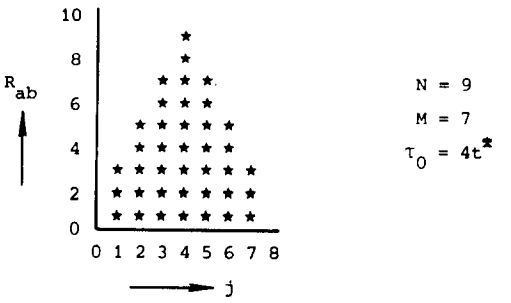

Figure 4. Sample of polarity correlation.

incremental frequency distribution. This function can be transformed into a frequency distribution of real chord lengths with the aid of [7].

The transformation of a chord length into a bubble diameter remains problematic, as a certain chord length can correspond to a small chord in a large bubble or a large chord in a small bubble, while moreover the velocity of the bubbles may differ. This problem can be overcome if the following assumptions, according to Thang & Davis (1979), are made:

—the bubbles are spherical
—the probe has equal probability to pierce any point on the projected frontal area of the bubbles
—all bubbles travel in the same direction with the same average velocity u_G.

If the probability density function of measured chord lengths is denoted by $g(l)$ and that of the detected bubble diameters by $f(d)$, it is shown by Herringe & Davis (1976) that

$$f(d) = \tfrac{1}{2}(g(l) - l\,g'(l)). \qquad [8]$$

The use of this equation to obtain the function $f(d)$ requires differentiation of function $g(l)$, which can cause substantial errors, due to inaccuracies in the experimentally determined distribution $g(l)$. It is shown by Van der Welle (1983), that the sampling frequency used is too low to obtain accurate distribution functions. On the other hand, some investigators report that bubbles which are not centrally pierced will tend to displace their center in such a way that anyhow the diameter is measured (cf. Buchholz *et al.* 1979). This point of view makes the analysis of Herringe and Davis, based on the second one of the above assumptions, rather doubtful. Hence it is assumed for the present case that the bubble diameter equals the measured chord length, so that $f(d) = g(l)$.

Integration of the probability density function yields a cumulative distribution function of bubble diameters, representing the percentage of the total number of measured bubbles whose diameter is below a given value, and thus forming another basis for defining a mean bubble diameter. Various definitions of mean bubble diameter are found in literature and are discussed in the Appendix.

A measure of the spread in measured diameters around the median diameter d_{50} is given by the geometric standard deviation s_g, defined as $s_g = \log (d_{84}/d_{50})$, or by the dispersion of the distribution, defined as the quotient d_{84}/d_{50}.

It must be noted here, that the distribution functions and mean diameters obtained are only representative of *detected* bubbles. The spectrum of detected bubbles will in general not be representative of the spectrum of all existing bubbles, as the probability for the probe to detect a bubble is inversely proportional to the cross-sectional area of the bubble, i.e. to d_b^2. If we denote the probability density function of the detected bubbles by $f(d)$ and that of all bubbles with centers passing through a unit area of the flow cross section by $j(d)$, it is shown by Herringe & Davis (1976) that

$$j(d) = k\frac{f(d)}{d_b^2}, \qquad [9]$$

where

$$k = \frac{4}{\pi}\frac{n_b}{N_b}$$

in which n_b is the number of detected bubbles and N_b is the total number of bubbles passing through a unit area. The value of k is not very important, as it is a constant and thus only influences the magnitude of the probability function, leaving the mean diameters unaffected. The function $j(d)$ will yield a much narrower bubble size range and much smaller mean diameters than those obtained from the function $f(d)$ due to the division by d_b^2.

3. DESCRIPTION OF TEST FACILITY

Except for the instrumentation, adapted to suit the present purpose, the air–water test facility was largely the same as previously used by Wisman (1979). In this test loop water is circulated by a centrifugal pump, whereas the air is blown once through the test section. The air is mixed with the water by injection through some 600 ferrules, special measures being taken to also ensure uniform distribution of the incoming water flowing around the ferrules. After this mixer and a flow straightener a pipe of 100 mm internal diameter with a straight mixing length of about 3 m (30 diameters) is available for further homogenization of the two-phase flow before it enters the test section proper. This section consists of a straight perspex pipe of 100 mm i.d. The test loop is equipped with a probe assembly of the design shown in figure 1. The probe holder is mounted on a traversing unit attached to the test

section about 3.5 m above the mixer. The holder enters the pipe through a leak-tight ferrule and traverses along a diametral chord.

4. MEASUREMENTS

4.1. *Flow conditions*

A wide range of flow velocities for each of the phases appeared desirable, as did the possibility to compare our results with data obtained earlier in the same test facility. Hence the set of 25 mixture adjustments used by Wisman (1979) and Timmermans (1979) were chosen as a basis for the present experiments. This set consists of five superficial liquid velocities: 0.9, 1.3, 1.7, 2.1 and 2.5 m/s, each combined with five nominal void fractions, 0.25, 0.38, 0.50, 0.63 and 0.75. These adjustments are coded by a serial number consisting of two figures:

—the first figure refers to the superficial water velocity:
1 stands for the lowest (0.9 m/s) and
5 stands for the highest velocity (2.5 m/s)
—the second number refers to the nominal void fraction:
1 stands for the lowest (0.25) and
5 stands for the highest (0.75) nominal void fraction.

Table 1 uses these serial numbers to list the 15 mixture adjustments selected for the present measurements. According to the flow pattern map of Hewitt and Roberts (1969) the flow conditions are in the plug flow region, except for $\alpha = 0.75$, but close to the bubble flow region. The conditions for $\alpha = 0.75$ are close to the churn flow regime. The observed flow patterns, however, differed slightly from these predicted ones, in that they ranged from bubble flow at low void fractions to froth flow at the highest void fraction. These minor differences may be attributed, e.g. to the relatively large pipe diameter used in the present study.

4.2. *Results*

4.2.1. *Void fraction.* The void fraction measurements by resistivity probe are checked by comparison with void fraction values obtained by a γ-photon attenuation technique. Figure 5 shows the measured void fractions for some typical adjustments, viz. serial numbers 31 through 35, obtained by photon attenuation and probe, respectively. The fluctuations in the curves representing the photon attenuation data are caused by oscillations in the 12th degree polynomials used to represent the measured values (cf. Wisman 1979). Hence they do not represent a physical phenomenon and are obviously absent from the probe data. Apart from the above polynomial-induced fluctuations the shapes of the two sets of curves are seen to be in good agreement, the agreement improving for the higher void fractions. This is borne out by the comparison of the cross-sectional averages shown in table 2. The deviations of $\langle \alpha_p \rangle$

Table 1. Flow condition data

u_{sl} \ $\langle\alpha\rangle$	0.25	0.38	0.50	0.63	0.75
0.9					
1.3	21 (0.6)	22 (1.2)	23 (2.7)	24 (4.9)	25 (9.9)
1.7	31 (0.7)	32 (1.5)	33 (3.2)	34 (5.6)	35 (10.7)
2.1	41 (0.9)	42 (1.7)	43 (3.6)	44 (6.2)	45 (12.4)
2.5					

Note: Bracketed values refer to the superficial gas velocity.

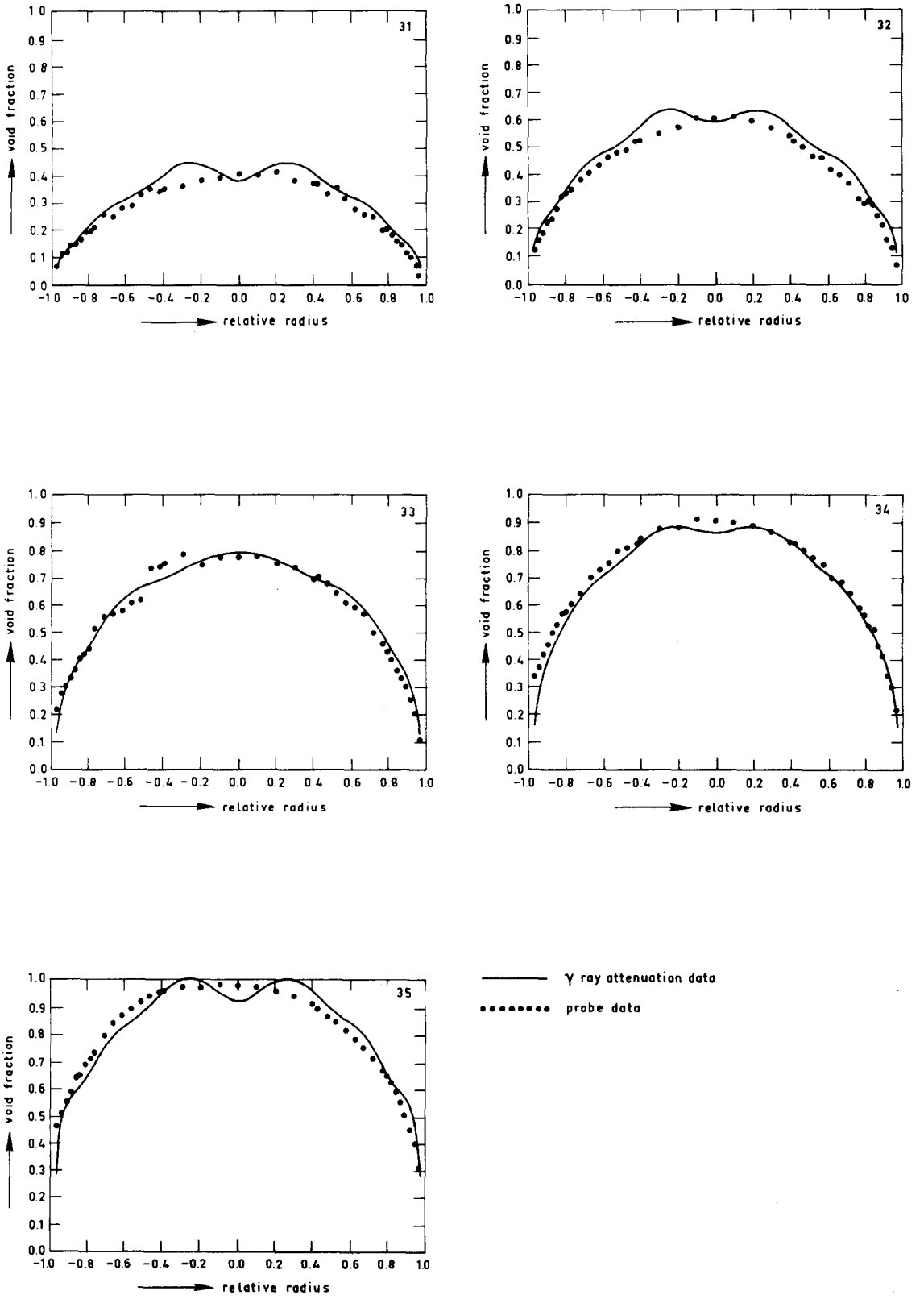

Figure 5. Radial distributions of void fraction.

Table 2. Averaged void fractions

serial number	$\langle\alpha_p\rangle$	$\langle\alpha_\gamma\rangle$	$d\alpha_p$ [%]
21	0.282	0.281	0.3
22	0.361	0.404	-10.6
23	0.473	0.524	- 9.7
24	0.615	0.607	1.3
25	0.726	0.714	1.7
31	0.242	0.273	-11.4
32	0.363	0.406	-10.6
33	0.505	0.520	- 2.9
34	0.619	0.600	3.2
35	0.724	0.731	- 1.0
41	0.235	0.282	-16.7
42	0.364	0.408	-10.8
43	0.482	0.531	- 9.2
44	0.605	0.653	- 7.3
45	0.732	0.775	- 5.5

with respect to $\langle\alpha_\gamma\rangle$ most likely originate from improper accounting for the dewetting time. Hence the first part of the delay time as well as signals from small bubbles or droplets are not taken into account. At high void fractions this effect is likely to be compensated by the effect of closely joining bubbles being detected as one single bubble. This is borne out by the decreasing values of the deviation $d\alpha_p$ shown in the table. Measurement 21 forms an exception to this trend, probably due to the inherent difficulty of obtaining identical gas mass flows at these very low set points.

A point worth noting for the probe measurements is their applicability for high void fractions (cf. adjustment 35). This is due to the fact that the stainless steel tube of the probe holder serves as second electrode. This design obviates the need for the conducting phase (i.e. the liquid) to be continuous, often mentioned as prerequisite in the relevant literature.

Although a number of references can be found in literature concerning local void fraction measurements, little is known about empirical correlations for predicting local void fractions. This is probably due to the wide variation in possible flow patterns (bubble, plug, annular, mist flow) and their associated void fraction distributions. For the higher void fractions parabolic-shaped distributions are commonly found, as in the present author's measurements, but for low qualities (bubble flow) the results differ. For void fractions up to 0.5 and superficial liquid velocities lower than about 2 m/s so-called "saddle-shaped" void fraction distributions, showing a local minimum at the pipe centerline, are usually observed (cf. e.g. Nassos 1963, Malnes 1966, Petrick & Kudirka 1966, Serizawa *et al.* 1975 and Herringe & Davis 1976). In general, these investigators assumed that the void fraction distribution strongly depended on the inlet geometry.

Conversely, no saddle-shaped distributions were found by the present author and by Wisman (1979), for measurements in the bubble and plug flow regime. Just as well, measurements by Thang & Davis (1979) on the structure of bubbly flows through venturis, performed in the same test facility of Herringe and Davis, did not show saddle-shaped profiles downstream of the venturi exit. Rather, these distributions all tended towards a pattern with a maximum at the pipe centerline, most likely due to the stronger turbulent mixing.

The latter results were confirmed by Sekoguchi *et al.* (1981) who observed both the parabolic and the saddle-shape profiles after a mixing length of 140 D under the same flow condition in the same test section, but with different air–water mixers. They suggest that the

difference in bubble size distribution governs which type of profile appears. It was also found that the type of distribution is dependent on the magnitude of liquid velocity.

Differences such as those just described impede the development of void fraction distribution functions covering a wide range of qualities. In the following an attempt is made to find a distribution function for the present author's results, i.e. for the void fraction range from about 0.25 to 0.75. Following other investigators, e.g. Bankoff (1960), Petrick & Kudirka (1966), Herringe & Davis (1976), a power law function:

$$\alpha = \alpha_{max}\left(1 - \frac{2r}{D}\right)^{1/n} \qquad [10]$$

is proposed, similar to that describing the velocity profiles in single-phase turbulent pipe flow.

Although α_{max} in [10] is available from the measured values, use is made of the cross-sectionally averaged values of all void fraction data to determine the power $1/n$, since this not only improves the approximation, but also follows engineering practice, where the averaged value is known rather than a maximum value. The cross-sectional averaged void fraction is obtained from the definition:

$$\langle\alpha\rangle = \frac{1}{A}\int \alpha \, dA$$

with α according to [10]. Elaboration yields the well-known formula:

$$\langle\alpha\rangle = \frac{2\,\alpha_{max}}{(1/n + 1)(1/n + 2)}.$$

Substituting [10] yields

$$\alpha = \langle\alpha\rangle \frac{1}{2}\left(\frac{1}{n} + 1\right)\left(\frac{1}{n} + 2\right)\left(1 - \frac{2r}{D}\right)^{1/n}. \qquad [11]$$

Using this equation for all measured void fraction distributions, the following best fit is obtained for the power $1/n$:

$$\frac{1}{n} = \left(\frac{1 - \langle\alpha\rangle}{2}\right)^{0.7}. \qquad [12]$$

Figure 6 shows the measured void fractions (taken from figure 5) compared with the approximation by the power law of [11] and [12]. The agreement is excellent except near the centerline where the power law shape is slightly too peaked. For high values of the cross-sectionally averaged void fraction local void fractions in the vicinity of the centerline become greater than 1, which is physically impossible. This is further elaborated in table 3 where it is shown that α_{max} starts to exceed 1 for $\langle\alpha\rangle > 0.7$. For $\langle\alpha\rangle$ equals 1, $1/n$ becomes zero, hence $\alpha = \langle\alpha\rangle = 1$, which is physically correct. It should be stressed that application of [12] is limited to the range of experimental conditions shown in table 1.

Although the superficial liquid velocity ranged from 1.3 to 2.1 m/s in our measurements, no dependence on this velocity could be detected. This also holds for the measurements of Wisman. These findings are at variance with the results of Petrick & Kudirka (1966) who approximated their measured data by

$$\frac{1}{n} = \frac{0.024}{\langle\alpha\rangle} u_{sl}^{2/3}, \qquad [13]$$

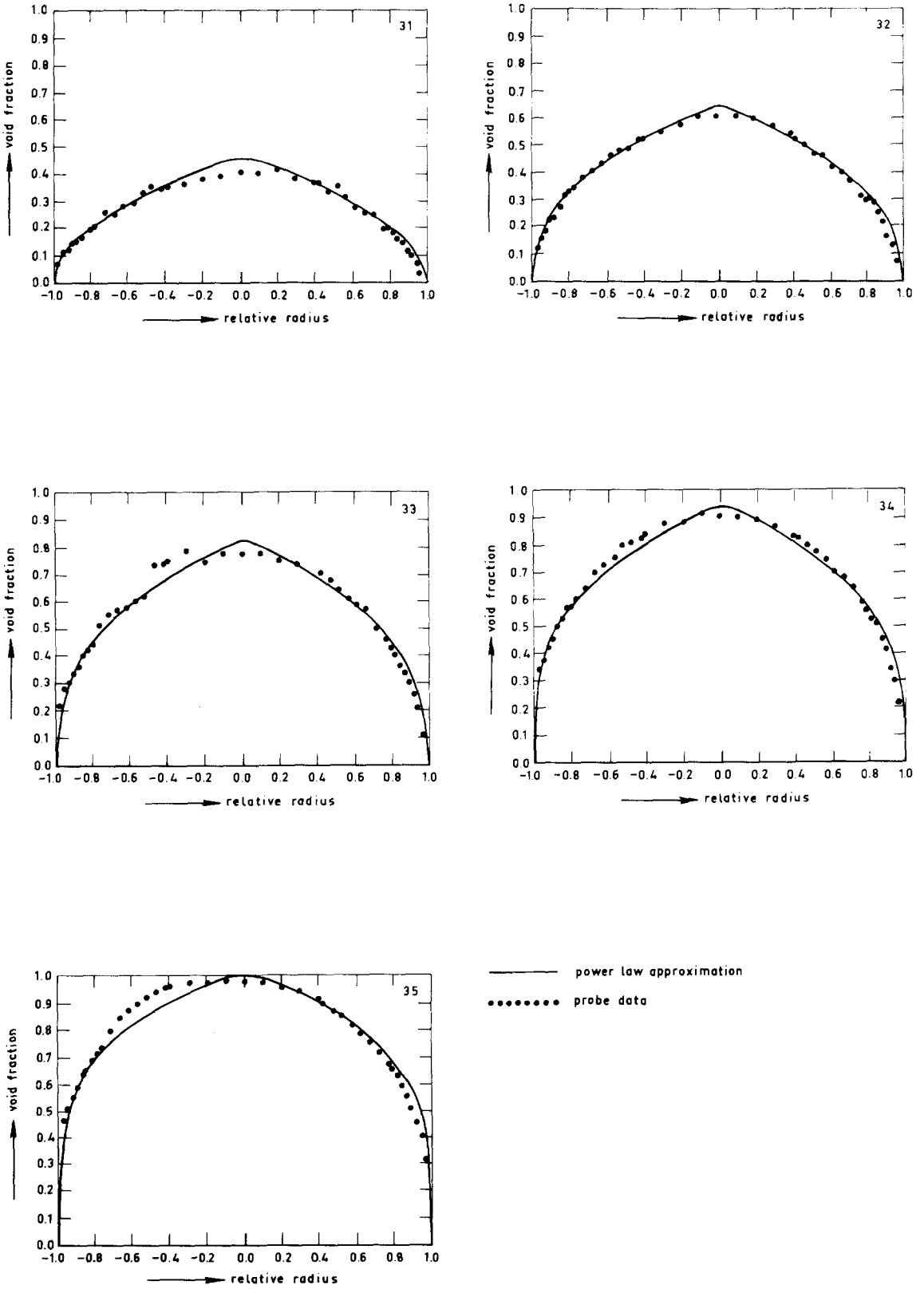

Figure 6. Measured void fractions with power law approximation.

Table 3. Power law data

<α>	α_{max}	n from equation (12) ★)	n from equation (13)
0.0	0.0	(1.62)	0.0
0.1	0.202	(1.75)	1.32
0.2	0.386	1.90	2.65
0.3	0.550	2.09	3.97
0.4	0.695	2.32	5.30
0.5	0.820	2.64	6.62
0.6	0.923	3.09	7.92
0.7	1.003	3.77	9.27
0.8	1.055	5.01	10.60
0.9	1.073	(8.14)	11.92
0.95	1.060	(13.23)	12.59
1.0	1.000	(∞)	13.25

★) *Bracketed values refer to <α> beyond the range investigated by the present author.*

where the superficial velocity u_{sl} is given in ft/s. This equation predicts much flatter void fraction profiles than [12], as illustrated in the last column of table 3 showing the value of n for $u_{sl} = 1.7$ m/s. This value for u_{sl} applies for the void fractions shown in figure 6 (cf. table 1). The discrepancy in the power $1/n$ may due to the difference in turbulent mixing between the two test sections. No further explanation is offered because of the author's ignorance of the details of Petrick and Kudirka's test loop.

4.2.2. *Bubble velocity.* Figure 7 shows the measured velocities of adjustments 31 through 35. The shape of the velocity profiles is seen to change from flat at low void fractions (number 31) to more or less sine shaped at high void fractions (number 35), which appeared to be independent of the superficial liquid velocity (cf. Van der Welle 1983). This change is to be expected since the flow will be annular at high void fractions; for this mode of flow the velocity at the centerline is much higher than in the liquid layer. An unlikely velocity profile is seen for the high flow adjustment 35, where the shape is flattened in the core region. The explanation is to be found in the combination of insufficient sampling frequency with the fact that the correlation function is obtained as a histogram. The former causes a shift of the top of the correlation function to lower values of time delay (i.a.v. to lower values of j, cf. figure 4), so that the resolution decreases. This leads to an increasing gap between the different velocity levels, which are obtained from the j values. Obviously the velocities in the core region do not come close enough to the next velocity level to cause a shift in the j value, hence the profile is flattened. It is clear that these velocities are subject to large errors.

Verification of the measured velocities was undertaken by comparing the averaged values $\bar{u}_{Gp}$ and $\bar{u}_{Gf}$, based on the probe measurements and the measured gas volume flow ϕ_{vg}, respectively, where $\bar{u}_{Gp}$ is defined as

$$\bar{u}_{Gp} = \frac{\int_A \alpha u_{Gp} \, dA}{\langle \alpha \rangle A} \qquad [14]$$

and

$$\bar{u}_{Gf} = \frac{\phi_{vg}}{\langle \alpha \rangle A}. \qquad [15]$$

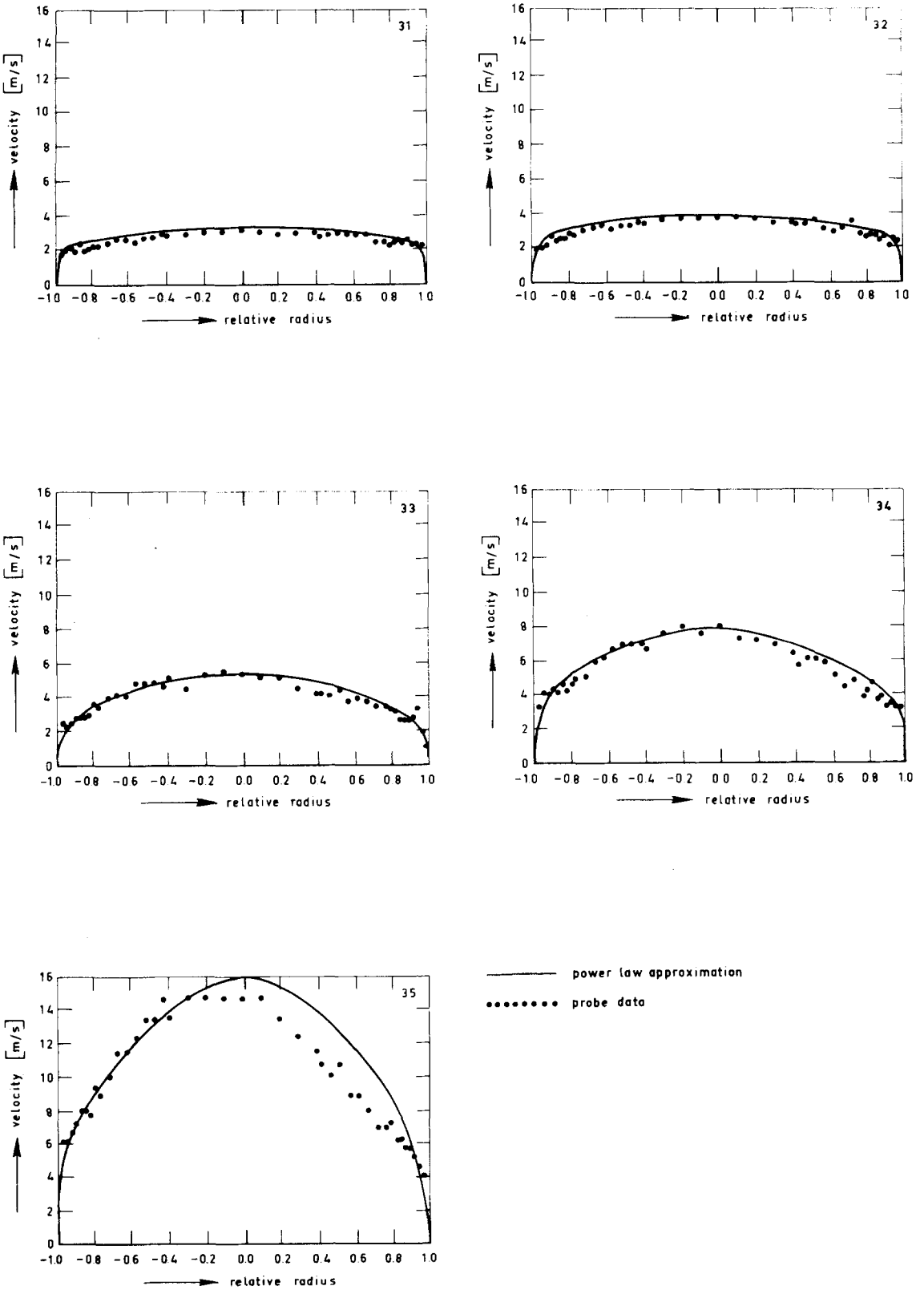

Figure 7. Radial distributions of velocities.

N.B. It is obvious that $\bar{u}_G$, which may also be written:

$$\bar{u}_G = \frac{\langle \alpha u_G \rangle}{\langle \alpha \rangle} \qquad [16]$$

will differ from the *cross-sectional* average of the local velocities:

$$\langle u_G \rangle = \frac{1}{A} \int_A u_G \, dA \qquad [17]$$

in value as well as in definition, as $\langle \alpha u_G \rangle \neq \langle \alpha \rangle \langle u_G \rangle$. Hence the velocity $\bar{u}_{Gf}$ computed from the measured gas volume flow according to [15] should not be compared with $\langle u_{Gp} \rangle$ computed from [17].

Furthermore the deviation of $\bar{u}_{Gp}$ with respect to $\bar{u}_{Gf}$ is computed:

$$d\bar{u}_{Gp} = \frac{\bar{u}_{Gp} - \bar{u}_{Gf}}{\bar{u}_{Gf}} 100\%. \qquad [18]$$

All values are plotted against $\langle \alpha \rangle$ in figure 8. The negative deviation of $\bar{u}_{Gp}$ with respect to $\bar{u}_{Gf}$ is seen to rise steeply with increasing void fraction. Adjustments 21 and 31 show a strong deviation from the general trends, which can be attributed to difficulties encountered with the adjustment and metering of these low gas flows as well as to the somewhat different flow pattern with respect to the other measurements. It was observed that areas of bubble flow were alternating with gas plugs moving at a different velocity and causing some reverse flow, which is not taken into account during the correlation procedure, so that in these cases the detected bubble velocity is bound to differ from the average gas velocity. The deviation of measurement 45 from the general trend is attributed to the measurement errors in the velocities discussed above.

The increasing negative values of $d\bar{u}_{Gp}$ for increasing void fractions are to be expected for a technique which measures the velocity of the discrete phase. This can be made plausible with the aid of figure 9, where the two probe signals are shown for both bubble and mist flow, i.e. for low and high void fraction, respectively. For bubble flow the signals are mainly high and the signal drops represent bubbles, while in case of droplet flow the signals are mainly low and peaks are caused by droplet contact. Correlation of both signals yields the gas velocity for bubble flow, whereas it will tend to predict the droplet velocity in case of mist flow. It is obvious that a continuous shift in the detected velocity from pure gas to a kind of liquid velocity will take place as the void fraction varies from low to high. Hence the measured velocity should be considered an *interface* velocity rather than a gas velocity. This is borne out by figure 10 in which $d\bar{u}_m$ is plotted against $\langle \alpha \rangle$, where $\bar{u}_m$ is defined (rather arbitrarily) as

$$\bar{u}_m = \frac{1}{2} (\bar{u}_{Gf} + \bar{u}_{Lf})$$

and

$$d\bar{u}_m = \frac{\bar{u}_{Gp} - \bar{u}_m}{\bar{u}_m} 100\%. \qquad [19]$$

For void fractions below about 0.55 it is found that $\bar{u}_{Gp} > \bar{u}_m$, because $\bar{u}_{Gp}$ is closer to the gas velocity, while for $\langle \alpha \rangle$ greater than about 0.55 $\bar{u}_{Gp} < \bar{u}_m$ because $\bar{u}_{Gp}$ is closer to the droplet velocity. The deviations $d\bar{u}_m$ plotted in figure 10 may be approximated by a straight line,

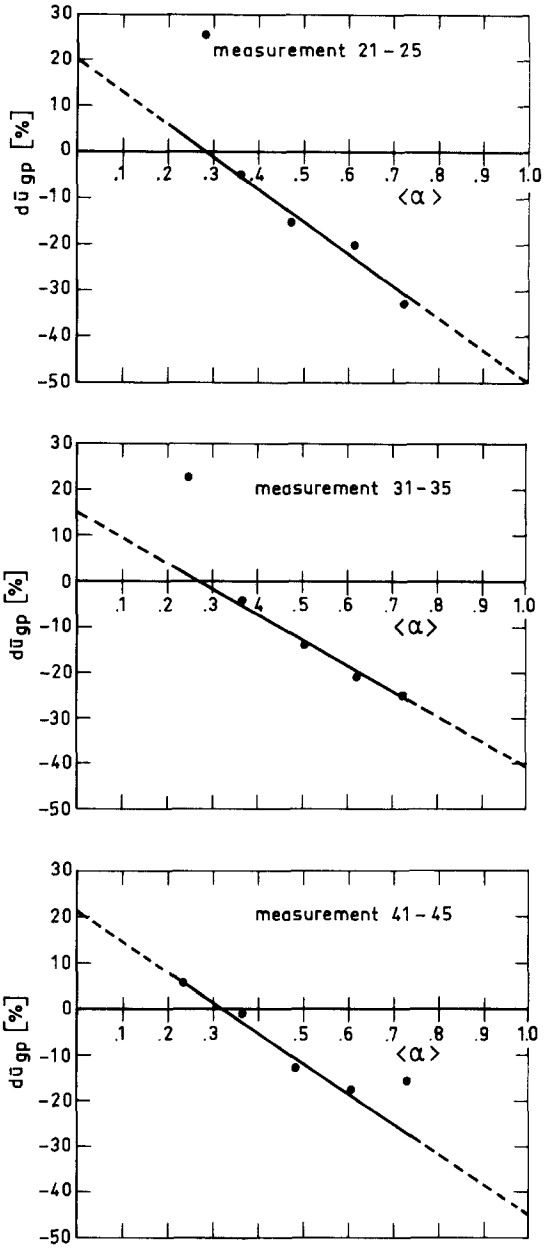

Figure 8. Deviation in measured velocity as a function of $\langle \alpha \rangle$.

according to a least squares fit. It seems reasonable to suppose that these lines should be more or less symmetrical with respect to the point $\langle \alpha \rangle = 0.5$, i.e. the deviations at $\langle \alpha \rangle = 0$ and $\langle \alpha \rangle = 1$ should be about equal with opposite sign. The figures more or less support this assumption. Of course the validation of the statement that an interface velocity is measured rather than a gas velocity can only be approximate, as use is made of averaged values for the velocities. The determination of any local mixture or interface velocity is impossible as no local liquid velocities are known.

From the considerations given in the preceding section it appears reasonable to approximate the distribution function of the measured velocities by a power law analogous to [11], yielding

$$u_{Gp} = \langle u_{Gp} \rangle \frac{1}{2}\left(\frac{1}{n} + 1\right)\left(\frac{1}{n} + 2\right)\left(1 - \frac{2r}{D}\right)^{1/n}. \qquad [20]$$

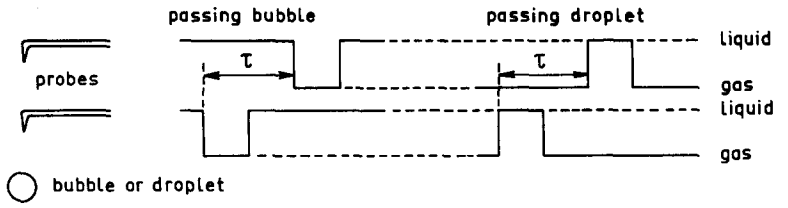

Figure 9. Probe signals for bubble and mist flow.

With the aid of the measured data the following correlation is established for the power $1/n$:

$$\frac{1}{n} = \frac{1}{10\,(1 - \langle\alpha\rangle)}. \qquad [21]$$

Again no dependence on the superficial liquid velocity was found, though such dependence might be expected from single-phase flow results. It should be emphasized that its absence may be simply due to insufficient accuracy of the available measurement data. Equation [21] is therefore merely suggested as a rule of thumb for a "rough-and-ready" approximation of the distribution shape.

In figure 7 the measured velocities are approximated by the power law of [20] and [21]. A good agreement is seen between the measured values and the proposed distribution function. At low void fractions the shape is very flat (for adjustment number 31 with $\alpha \approx 0.25$, [21] yields $n = 7.5$), but this shape becomes less flat with increasing void fraction (for

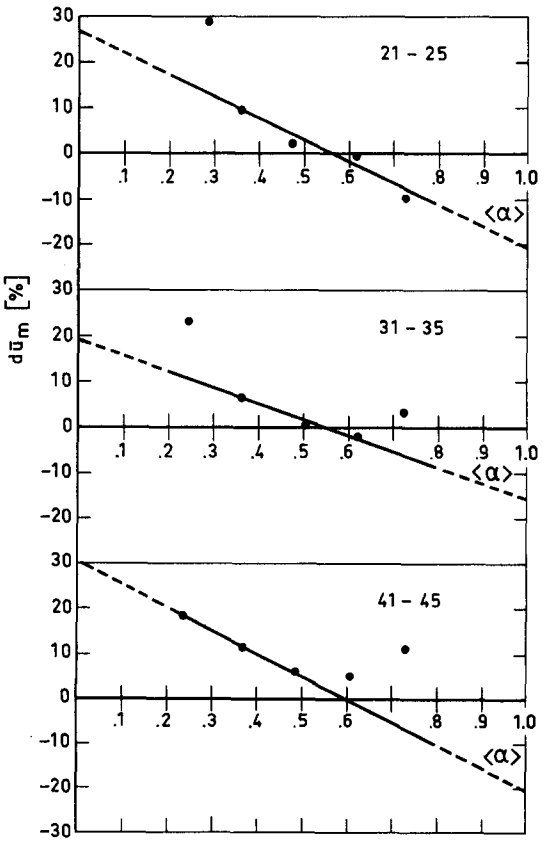

Figure 10. Deviation in $\bar{u}_m$ as function of $\langle\alpha\rangle$.

measurement 35, with $\alpha \approx 0.7$, $n = 3$). Adjustment 35 shows a certain asymmetry in measured values, most likely caused by disturbance of the flow by the probe holder.

It should be noted that very flat shapes at low void fractions are also found by other investigators, e.g. Malnes, Serizawa and Herringe. For $\alpha = 0.1$, e.g. [21] yields $n = 9$, which corresponds to the findings of Herringe & Davis.

Equation [21] yields incorrect results for $\alpha = 0$ and $\alpha > 0.9$, viz. $n = 10$ instead of about 7 for $\alpha = 0$ (single-phase flow) and $n = 0$ for $\alpha = 1$. Despite these imperfections the use of [21] is recommended as a practical rule of thumb for two-phase flows, which is of course only applicable within the range of experimental conditions shown in table 1.

4.2.3. *Bubble diameter.* In the absence of a predetermined idea on the relevance of the various mean bubble diameters defined in the Appendix, all eight diameters are plotted against the radius of the pipe.

Figure 11 shows the bubble diameters for adjustments 31 through 35. The dented shapes of the curves in this figure are attributed to the sample frequency, which was based on the requirement for velocity measurements and found inadequate for the determination of bubble size (cf. Van der Welle 1983). The resulting errors in the most frequent diameter (found at the top of the diameter frequency distribution), are about 20% to 40%.

The other diameters are in general somewhat less dented, i.e. the deviations are smoothed, as those diameters are obtained by arithmetical operations. In the plot of measurement 31 the curves of d_{gm} and d_{50} are seen to coincide for the most part. It is known from theory that the log-normal distribution of particle sizes has the property that d_{gm} equals d_{50} (see, e.g. Masters 1972). Although this fact may not be stated in reverse, it is quite likely that the diameter distribution function has indeed a log-normal shape. At the higher adjustments d_{gm} is still roughly equal to d_{50} in the wall region, but differs from d_{50} in the core region. This is by no means surprising as in that region the flow is far from bubbly and the detected diameters are hence of doubtful physical meaning.

Another interesting comparison is that of d_{am} with $d_{\alpha n}$, who should be equal as explained in the Appendix. Figure 11 shows a generally large discrepancy between both diameters, $d_{\alpha n}$ being 2 to 3 times greater than d_{am}, except for the region close to the wall, were indeed $d_{am} \approx d_{\alpha n}$. The deviation between d_{am} and $d_{\alpha n}$ is again due to insufficient sampling frequency, resulting in too low counts as successive bubbles are detected as one large bubble. The effect is twofold, viz. $d_{\alpha n}$ becomes too large (cf. [A6]) and the diameter distribution function shifts to higher diameter values. As the number of classes of this function is limited to 25, the additional consequence is a peak at the highest (25th) class, where all diameters greater than class 24 are accumulated. This means that the computed mean diameters (cf. the appendix) will tend to lower values as no class greater than 25 is taken into account. These two effects (shift to higher diameter values and a limit on the maximum diameter) apparently more or less cancel out when the diameters d_{am}, d_{gm}, d_{vm} and d_s are computed, hence these values can be considered fairly reliable. For the area in which $d_{\alpha n} \approx d_{am}$ it appeared from the probability density functions that only a small number of bubbles is present in class 25, thus confirming the above remarks on sampling frequency and number of classes of the distribution function.

As mentioned in subsection 2.4.3 the results thus obtained only hold for *detected* bubbles. An impression of the spectrum of all existing bubbles per unit area is obtained from equation [9]. The resulting diameter values for the same measurements 31 through 35 are shown in figure 12, from which it is seen that the diameters are significantly reduced. It is obvious that the diameter distribution function will be strongly skewed to the left. The top of this function is now mostly found in class 1, hence the first part of the function has a poor resolution. The influence of the sampling frequency is seen in some curves, viz. for measurement 32 at position $\pm 0.4\ R$ and for measurement 33 at position $\pm 0.8\ R$. At these locations the sample frequency was doubled in order to obtain reliable velocity measurements, yielding a sudden

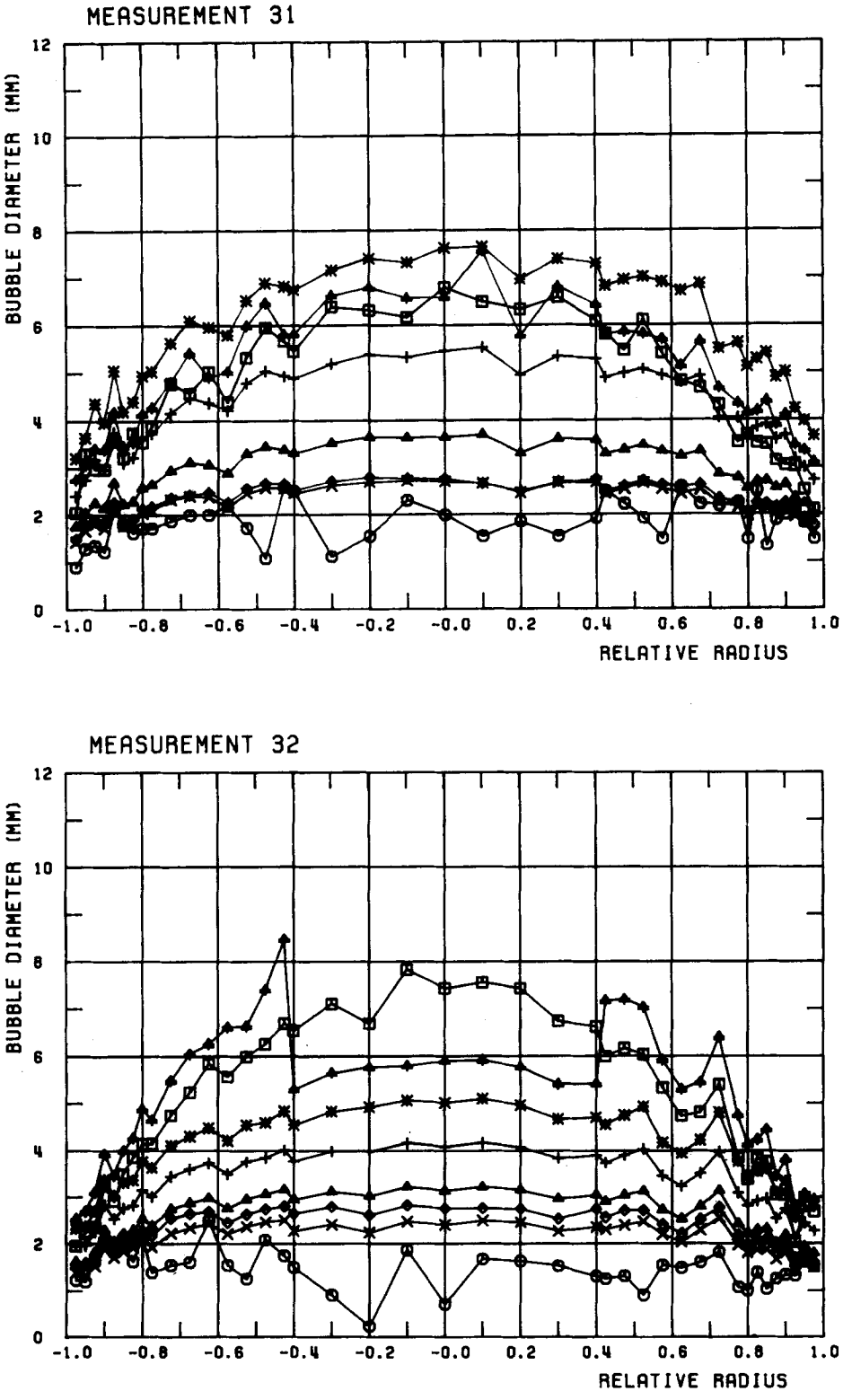

Figure 11. Radial distribution of detected bubble diameters.

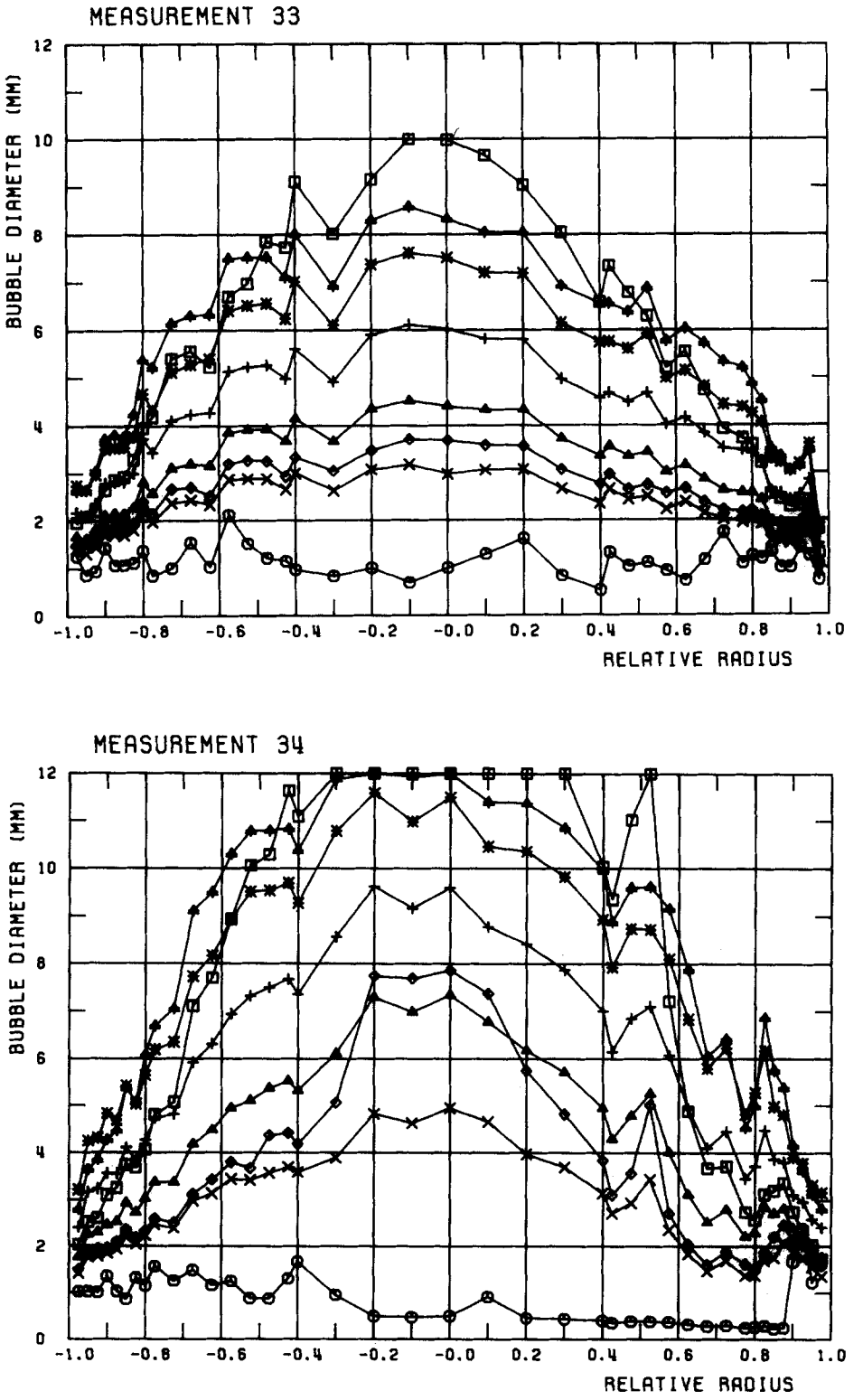
MEASUREMENT 33
BUBBLE DIAMETER (MM)
0
2
4
6
8
10
12
-1.0
-0.8
-0.6
-0.4
-0.2
-0.0
0.2
0.4
0.6
0.8
1.0
RELATIVE RADIUS
MEASUREMENT 34
BUBBLE DIAMETER (MM)
0
2
4
6
8
10
12
-1.0
-0.8
-0.6
-0.4
-0.2
-0.0
0.2
0.4
0.6
0.8
1.0
RELATIVE RADIUS

Figure 11 B.

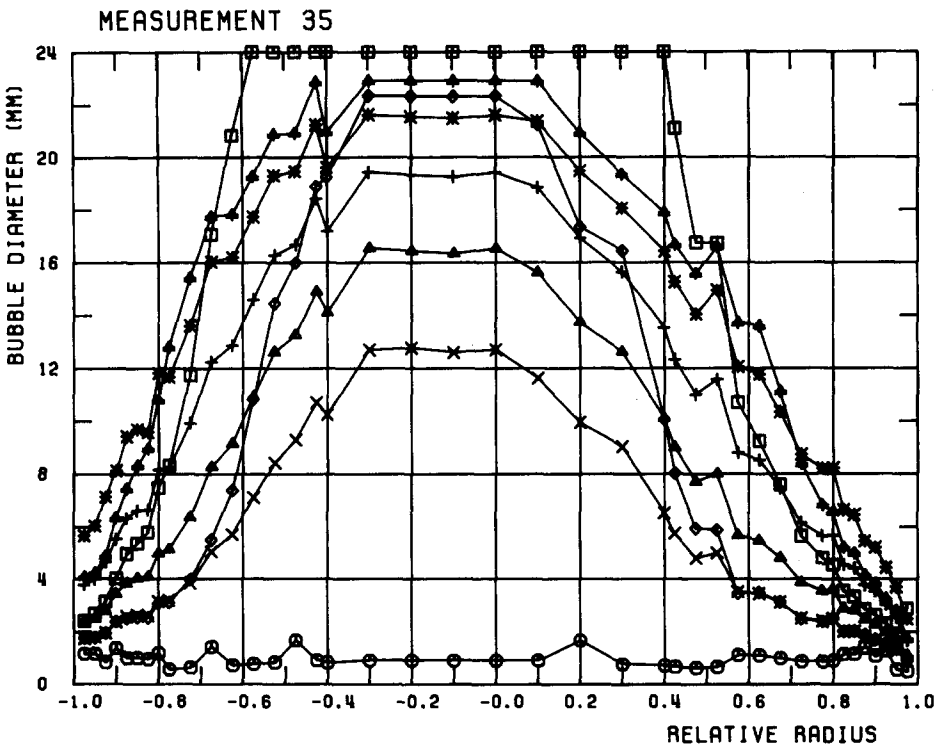

Figure 11 C.

decrease in bubble diameters. Again the diameters d_{gm} and d_{50} are roughly the same, with d_{gm} now slightly higher than d_{50}.

Some sort of verification of the measured bubble diameters was attempted by comparison with theoretically predicted diameters. These are obtained from a model suggested by Wisman (1979), which is based on a model for drop diameters given by Hinze (1955). While the reader is referred to the original text for a full description of the model, the resulting equations will be given here for the sake of completeness. The model yields an expression for the bubble diameter:

$$d_b = \left(\frac{\sigma \mathrm{We}_{\mathrm{cr}}}{2\,(1-\alpha)\rho_L}\right)^{0.6} \epsilon^{-0.4} \qquad [22]$$

in which σ is the surface tension and ρ_L is the density of the liquid. For the actual air–water flows the critical Weber number $\mathrm{We}_{\mathrm{cr}} = 2.43$. An expression for the energy dissipation ϵ was obtained by Wisman from the mechanical energy balance for a nonaccelerating flow on the assumption that the dissipation of turbulence energy in the flow is equal to its production. He further stated that the production of turbulence energy is due to the relative movement of the phases, i.e. the drag force plus the wall friction. The mechanical energy equation is obtained by multiplying the gas momentum equation by u_G, the liquid momentum equation by u_L and adding the products. The turbulence energy dissipation then yields

$$\epsilon = \frac{F_D\,(u_G - u_L) + \left(\dfrac{\mathrm{d}p}{\mathrm{d}z}\right)_{\mathrm{fr}} u_L}{(1-\alpha)\rho_L} \qquad [23]$$

in which F_D is the drag force and $(\mathrm{d}p/\mathrm{d}z)_{\mathrm{fr}}$ represents the pressure drop due to wall friction. As one-dimensional equations are used, the model predicts one-dimensionally averaged diameters; these were computed for all measurements of concern and are listed in table 4.

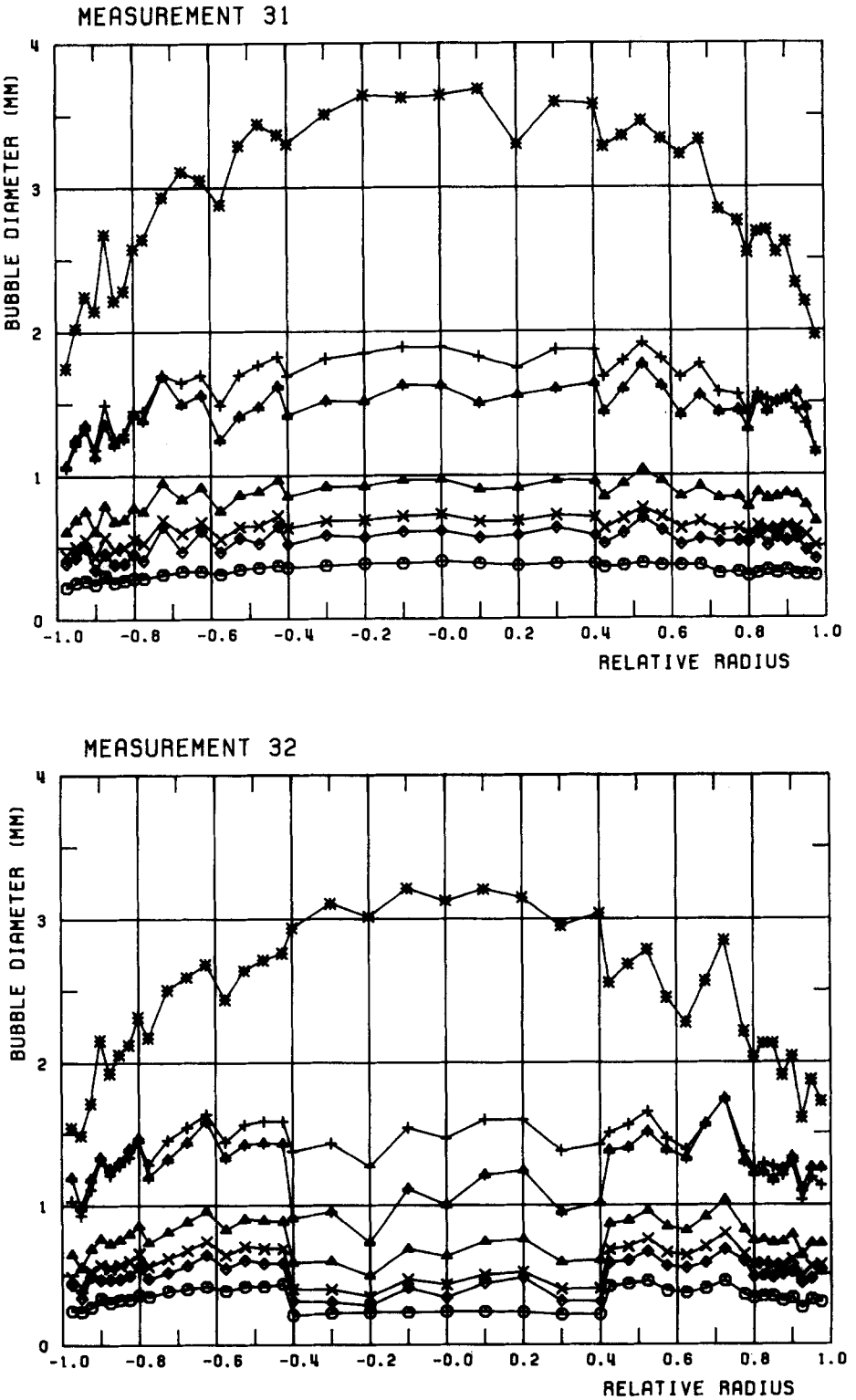

Figure 12. Radial distribution of existing bubble diameters.

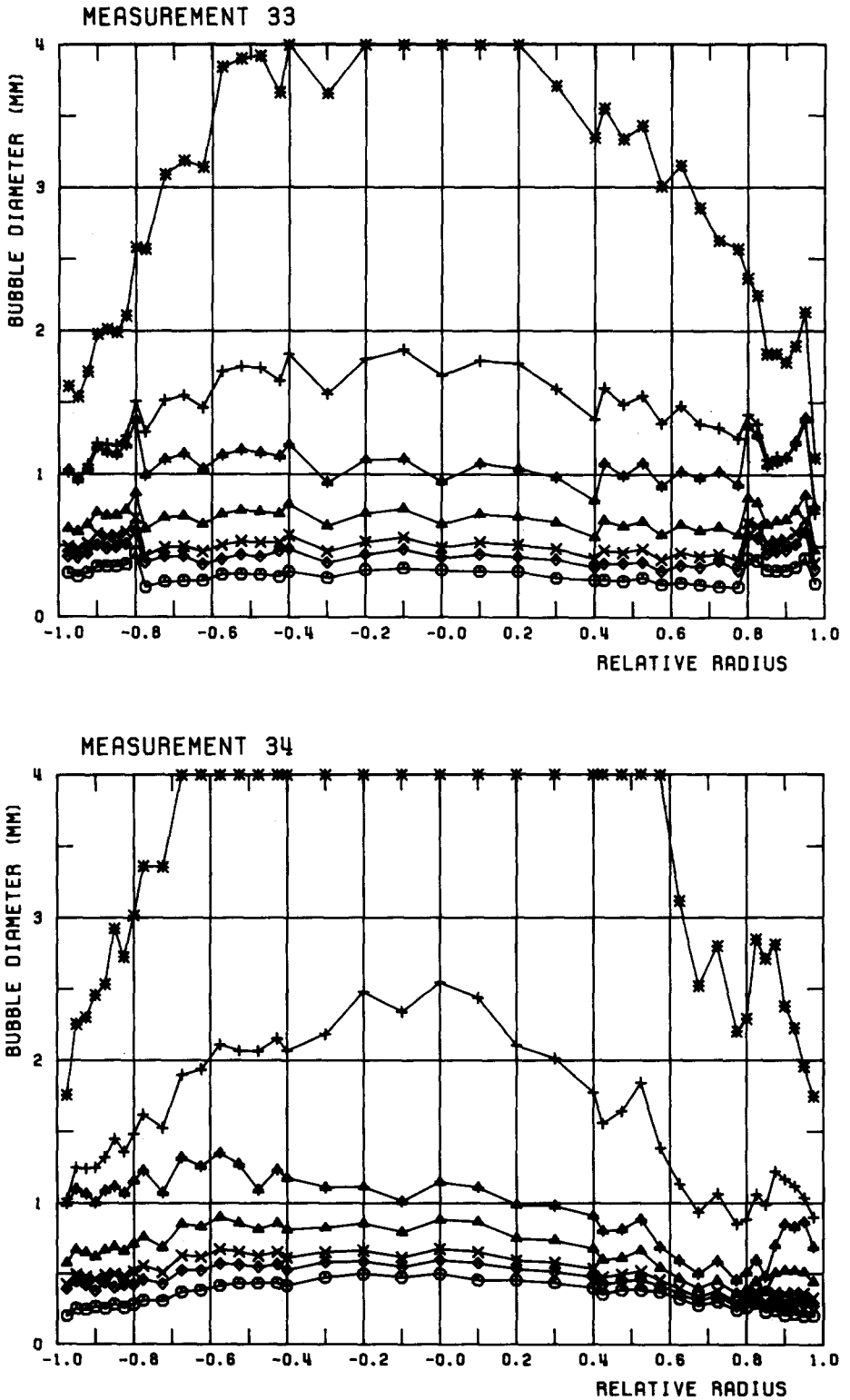
MEASUREMENT 33
BUBBLE DIAMETER (MM)
0
1
2
3
4
-1.0
-0.8
-0.6
-0.4
-0.2
-0.0
0.2
0.4
0.6
0.8
1.0
RELATIVE RADIUS
MEASUREMENT 34
BUBBLE DIAMETER (MM)
0
1
2
3
4
-1.0
-0.8
-0.6
-0.4
-0.2
-0.0
0.2
0.4
0.6
0.8
1.0
RELATIVE RADIUS

Figure 12 B.

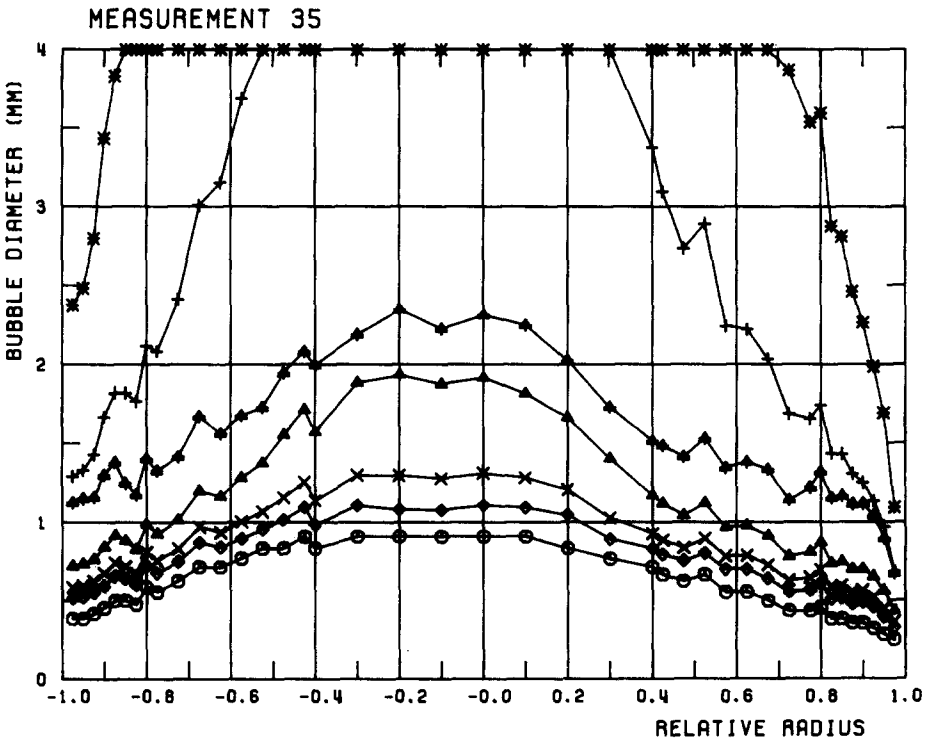

Figure 12 C.

The predicted diameters compare reasonably well with the Sauter mean diameter, except for high void fractions. This is illustrated in figure 13, in which two Sauter diameters per adjustment are plotted, viz. a high and a low value (cf. also table 4). The low values are obtained by neglecting the last (25th) class of the distribution function as these diameters are somewhat suspect for the reason stated earlier. The deviation between predicted and measured diameters is significant at higher void fractions. This is highly plausible as in this case the flow will be annular rather than bubbly, which means that the model looses its physical basis and that the detected "bubble" diameter is rather a slug diameter. It is thus

Table 4. Bubble diameter data

serial number	d_{model}	$\langle d_s \rangle$	$\langle d_{s\ min} \rangle$	dispersion	s_g
21	3.71	2.71	2.29	2.55	0.41
22	2.58	2.87	2.37	2.41	0.38
23	2.08	2.47	1.98	2.24	0.35
24	1.72	3.25	2.38	2.40	0.38
25	1.23	4.76	3.17	2.03	0.31
31	3.20	2.93	2.40	2.76	0.44
32	2.65	2.35	1.99	2.56	0.41
33	1.86	2.78	2.14	2.50	0.40
34	1.37	3.65	2.60	2.19	0.34
35	0.99	6.84	4.41	2.00	0.30
41	2.40	2.48	2.14	2.45	0.39
42	1.91	2.60	2.19	2.26	0.35
43	1.48	3.01	2.32	2.05	0.31
44	1.17	4.26	3.12	2.14	0.33
45	0.91	8.13	5.40	1.89	0.28

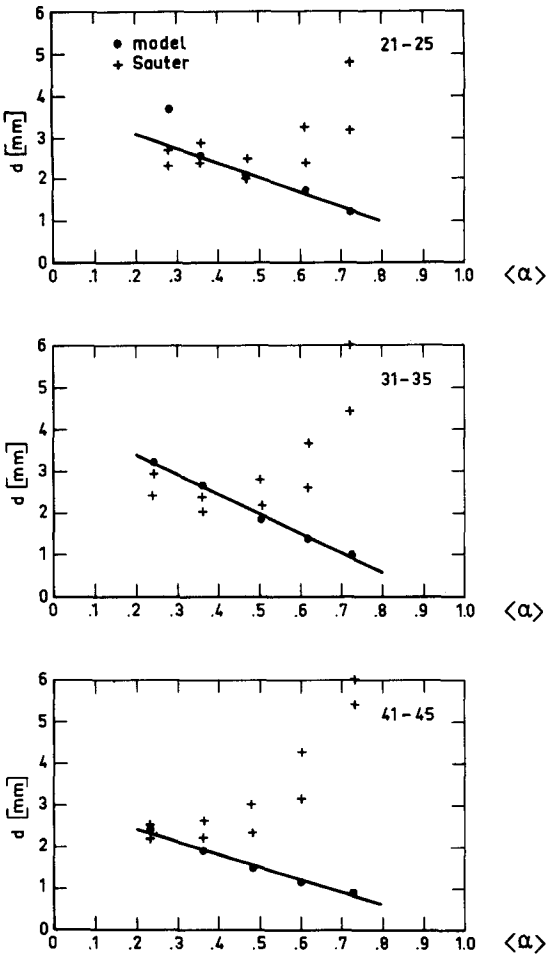

Figure 13. Bubble diameters versus void fraction.

seen that the model yields a good prediction of the Sauter mean diameter in bubbly flow ($\alpha <$ ca. 0.5) for the spectrum of all existing bubbles. If only the distribution of detected bubbles is known, i.e. no transformation according to [9] is performed, the model predicts the arithmetic mean diameter. Equation [9] yields

$$j(d_i) = k\frac{f(d_i)}{d_i^2} \quad \text{for } i = 1\ (1)\ n.$$

If we denote the Sauter diameter from the j function (existing diameters) as d_s^*, definition [A4] yields

$$d_s^* = \frac{\sum_{i=1}^{n} d_i^3 j(d_i)\,\Delta d_i}{\sum_{i=1}^{n} d_i^2 j(d_i)\,\Delta d_i} = \frac{\sum_{i=1}^{n} d_i^3 f(d_i)\,\Delta d_i/d_i^2}{\sum_{i=1}^{n} d_i^2 f(d_i)\,\Delta d_i/d_i^2} = \frac{\sum_{i=1}^{n} d_i f(d_i)\,\Delta d_i}{\sum_{i=1}^{n} f(d_i)\,\Delta d_i} \qquad [24]$$

which is the definition of d_{am} for the f function (detected diameters).

5. SUMMARY AND CONCLUSIONS

The present measurements in two-phase air–water flows are complementary to the results found in literature in that their ranges of void fractions and superficial liquid velocities extend up to 0.75 and 2.1 m/s, respectively, thus covering various flow patterns.

Reliable values were obtained for the local void fraction over the entire range $0 \leq \alpha \leq 1$. The distribution of the void fraction can, with fair accuracy, be described by a power law.

The resistivity probes used measure the velocity of the interface between the conducting and nonconducting phases. The shape of this interface velocity is well fitted by a power law, the exponent of which varies more strongly than for single-phase pipe flow.

The spectrum of measured bubble sizes can be converted into a spectrum of existing bubble sizes. It appears that the Sauter mean diameter computed from this existing spectrum is reasonable well predicted by the energy balance based model [22], provided the measurements refer to bubbly flow (i.e. void fractions up to 0.5).

The accuracy of the resistivity probe measurement technique should be improved in order to be able to measure higher velocities and to determine reliable bubble size distributions. Such improvement can be achieved by a decreased distance between the probe tips, combined with a more than proportional increase in sampling frequency. The data processing requirements resulting from the above recommendations suggest the use of a dedicated minicomputer instead of a microprocessor.

Acknowledgment—The work presented here forms part of a Ph.D. thesis published at Delft University of Technology. The author wishes to express his gratitude to his supervisor, Professor Ir. D.G.H. Latzko, for his continuing advice and encouragement. He is also particularly indebted to Mr. A. Korving for the design of the instrumentation (in hard- and software) and for the automation and operation of the test loop, as well as for discussions and valuable suggestions concerning this study.

APPENDIX

Definitions of bubble diameter

The following definitions for mean diameter have i.a. been reported in literature, mainly in the field of drop size distributions in sprays (cf. e.g. Mugele & Evans 1951), and are used here in the evaluation of bubble diameter data.

Most frequent diameter d_{mf}. This diameter is found at the top of the probability density function of diameters. A proper determination of this top requires a high sample frequency, even one substantially higher than the sampling frequency used for the velocity measurements. For the maximum sample frequency of 16 kHz significant errors in the determination of the most frequent diameter can be expected.

Arithmetic mean diameter d_{am} This diameter is defined as the sum of the diameters of the separate bubbles divided by the number of bubbles, hence:

$$d_{am} = \frac{\sum_{i=1}^{n} d_i f(d_i)\, \Delta d_i}{\sum_{i=1}^{n} f(d_i)\, \Delta d_i}, \qquad [A1]$$

where n = number of classes, d_i = the diameter of the ith class, $f(d_i)$ = the number of bubbles in that class, Δd_i = the size-class increment, which is uniform in our case.

Geometric mean diameter d_{gm}. This diameter is defined as the n_bth root of the product of the diameters of the n_b measured bubbles, which definition can conveniently be described in terms of logarithms as

$$\ln d_{gm} = \frac{\sum_{i=1}^{n} \ln d_i f(d_i)\, \Delta d_i}{\sum_{i=1}^{n} f(d_i)\, \Delta d_i}. \qquad [A2]$$

Volume mean diameter d_{vm}. This diameter is based on the volume rather than on the number of bubbles:

$$d_{vm} = \left(\frac{\sum_{i=1}^{n} d_i^3 f(d_i)\, \Delta d_i}{\sum_{i=1}^{n} f(d_i)\, \Delta d_i} \right)^{1/3}. \qquad [A3]$$

Volume-surface or Sauter diameter d_s. This diameter is mainly used in the field of mass transfer, as the volume represents the concentration of the material and the surface its contact area. The definition yields

$$d_s = \frac{\sum_{i=1}^{n} d_i^3 f(d_i)\, \Delta d_i}{\sum_{i=1}^{n} d_i^2 f(d_i)\, \Delta d_i}. \qquad [A4]$$

Median diameter d_{50}. This diameter is defined as the diameter above or below which 50% of the number of bubbles lie, and is thus easily obtained from the cumulative distribution function. If the probability density function is a log-normal distribution the median diameter corresponds to the geometric mean diameter. In the same way as the definition of d_{50} other diameters can be defined, e.g. d_{84}, which corresponds to the diameter one standard deviation distant from the median diameter, provided that the bubble diameter density function can be represented by log-normal distribution.

Diameter, based on void fraction and bubble frequency $d_{\alpha n}$. All the above mentioned mean diameters derive from bubble diameter distributions. It is also possible, however, to obtain a mean bubble diameter without the need to classify the various measured diameters, viz. from the measured void fraction and bubble frequency. The averaged number of samples per bubble $\bar{n}$ equals the total number of samples N multiplied by the void fraction α, yielding the number of samples in all bubbles, divided by the number of bubbles n_b; hence:

$$\bar{n} = \frac{N\alpha}{n_b}. \qquad [A5]$$

After substituting [A5] into [7] the averaged chord length $\bar{l}$ yields

$$\bar{l} = \frac{N\alpha u_G}{f n_b}. \qquad [A6]$$

In subsection 2.4.3 it is made plausible that the average bubble diameter is equal to this average chord length. As an averaging procedure is performed over the number of bubbles, it is obvious that the mean diameter thus obtained is identical to the arithmetic mean diameter d_{am}; the results obtained by [A6] should therefore be compared with the results of [A1].

NOMENCLATURE

- A cross-sectional area
- a, b probe signals
- c concentration
- D pipe diameter
- d diameter, deviation
- F volume force

F_{ab} cross-correlation function of signals a and b
f frequency
$f(d)$ probability function of detected bubble diameters
$g(l)$ probability function of measured chord lengths
i, j number
$j(d)$ probability function per unit area
l bubble chord length
M number of shifts
N total number (bubbles, samples)
p pressure
R_{ab} polarity correlation function of signals a and b
r radius
s standard deviation
T time
t time, period
u velocity
We Weber number $(\rho u^2 d)/\sigma$
x coordinate
z axial coordinate
α void fraction
ϵ energy dissipation
ρ density
σ surface tension
τ time delay
ϕ_m mass flow rate
ϕ_v volume flow rate

Subscripts

a arithmetic
b bubble
cr critical
D drag
fr frictional
G gas
g geometric
L liquid
m mean value
p probe
s Sauter diameter
sl superficial liquid
v volumetric
γ γ ray attenuation

REFERENCES

BANKOFF, S. G. 1960 A variable density, single fluid model for two-phase flow with particular reference to steam–water flow. *Trans. ASME, J. Heat Transfer* **82,** 265–272.

BUCHHOLZ, R., ZAKRZEWSKI, W. & SCHÜGERL, K. 1979 Messtechniken zur Bestimmung der Eigenschaften von Blasen in Blasensäulen. *Chemie-Ingenieur Technik* **51,** 568–575.

HERRINGE, R. A. & DAVIS, M. R. 1974 Detection of instantaneous phase changes in gas–liquid mixtures. *J. Phys. E.* **7,** 807–812.

HERRINGE, R. A. & DAVIS, M. R. 1976 Structural development of gas–liquid mixture flows. *J. Fluid Mechan.* **73,** 97–123.

HEWITT, G. E. & ROBERTS, D. N. 1969. Studies of two-phase flow patterns by simultaneous x-ray and flash photography. United Kingdom Atomic Energy Authority, AERE-M 2159.

HINZE, J. O. 1955 Fundamentals of the hydrodynamic mechanism of splitting in dispersion processes. *AIChE J.* **1,** 289–295.

JONES, O. W. & DELHAYE, J. M. 1976 Transient and statistical measurement techniques for two-phase flows: A critical review. *Int. J. Multiphase Flow* **3,** 89–116.

KORVING, A. 1979 Meetsysteem voor het bepalen van de dampvolumefraktie, de belgrootte-verdeling en de belsnelheid in een stromend lucht-water mengsel (in Dutch). EV-1104 (SWST-57), Laboratory for Thermal Power Engineering, Delft University of Technology.

KORVING, A. 1980 Digitale signaalconditionering voor de weerstandsprobe (in Dutch). SWST-memo-80/1, Laboratory for Thermal Power Engineering, Delft University of Technology.

MALNES, D. 1966 Slip ratios and friction factors in the bubble flow regime in vertical tubes. Kjeller report, KR–110.

MASTERS, K. 1972 *Spray drying.* Leonard Hill Books, London.

MUGELE, R. A. & EVANS, H. D. 1951 Droplet size distribution in sprays. *Ind. Eng. Chem.* **43,** 1317–1324.

PETRICK, M. & KUDIRKA, A. A. 1966 On the relationship between the phase distributions and relative velocities in two-phase flow. *Proc. 3rd Int. Heat Transfer Conference,* Chicago, 184–192.

SEKOGUCHI, K., FUKUI, H. & SATO, Y. 1981 Flow characteristics and heat transfer in vertical bubble flow. In: *Two-phase Flow Dynamics* (Edited by A.E. Bergles and S. Ishigai), 59–74 Hemisphere Publishing Corporation.

SERIZAWA, A., KATAOKA, I. & MICHIYOSHI, I. 1975 Turbulence structure of air–water bubbly flow. *Int. J. Multiphase Flow* **2,** 221–246.

THANG, N. T. & DAVIS, M. R. 1979 The structure of bubble flow through venturis. *Int. J. Multiphase Flow* **5,** 17–37.

TIMMERMANS, J. H. 1979 Meting van de lokale gasfraktie, gassnelheid en belgrootte in een verticale lucht-waterstroming met behulp van electrische weerstandssondes (in Dutch). EV-1112 (SWST-59), Laboratory for Thermal Power Engineering, Delft University of Technology.

VELTMAN, B. P. Th. & KWAKERNAAK, H. 1961 Theorie und Technik der Polaritätskorrelation für die dynamische Analyse niederfrequenter Signale und Systeme. *Regelungstechnik* **9,** 357–400.

WELLE, R. VAN DER 1983 A contribution to the numerical description of rotating two-phase flow. Ph.D. thesis, Laboratory for Thermal Power Engineering, Delft University of Technology.

WISMAN, R. 1979 Fundamental investigation on interaction forces in bubble swarms and its application to the design of centrifugal separators. Ph.D. Thesis, Laboratory for Thermal Power Engineering, Delft University of Technology.

ZWAHR, H. 1976 Das Verhalten von Zwei-Phasen-Gemischen in Zentrifugalfeldren. Ph.D. Thesis, Technische Universität Hannover.